AFRL-AFOSR-VA-TR-2024-0052

Narrow-linewidth Brillouin laser source based on chalcogenide resonators in the mid-infrared region

Wounjhang Park
REGENTS OF THE UNIVERSITY OF COLORADO
3100 MARINE ST 572 UCB
BOULDER, CO,
US

12/01/2023
Final Technical Report

Air Force Research Laboratory
Air Force Office of Scientific Research
Arlington, Virginia 22203
Air Force Materiel Command

REPORT DOCUMENTATION PAGE

PLEASE DO NOT RETURN YOUR FORM TO THE ABOVE ORGANIZATION.

1. REPORT DATE	2. REPORT TYPE	3. DATES COVERED	
20231201	Final	START DATE 20190901	END DATE 20230831

4. TITLE AND SUBTITLE
Narrow-linewidth Brillouin laser source based on chalcogenide resonators in the mid-infrared region

5a. CONTRACT NUMBER	5b. GRANT NUMBER	5c. PROGRAM ELEMENT NUMBER
	FA9550-19-1-0364	61102F
5d. PROJECT NUMBER	**5e. TASK NUMBER**	**5f. WORK UNIT NUMBER**

6. AUTHOR(S)
Wounjhang Park

7. PERFORMING ORGANIZATION NAME(S) AND ADDRESS(ES)
REGENTS OF THE UNIVERSITY OF COLORADO
3100 MARINE ST 572 UCB
BOULDER, CO
US

8. PERFORMING ORGANIZATION REPORT NUMBER

9. SPONSORING/MONITORING AGENCY NAME(S) AND ADDRESS(ES)	10. SPONSOR/MONITOR'S ACRONYM(S)	11. SPONSOR/MONITOR'S REPORT NUMBER(S)
Air Force Office of Scientific Research 875 N. Randolph St. Room 3112 Arlington, VA 22203	AFRL/AFOSR RTB1	AFRL-AFOSR-VA-TR-2024-0052

12. DISTRIBUTION/AVAILABILITY STATEMENT
A Distribution Unlimited: PB Public Release

13. SUPPLEMENTARY NOTES

14. ABSTRACT
The ultimate goal of this project is to develop a narrow linewidth laser based on stimulated Brillouin scattering (SBS). Achieving narrow linewidth lasing in a portable, compact device platform is one of the outstanding challenges in the field of laser development, especially for military applications in which power, weight, size and robustness are critical. Chip-scale microresonators are the natural candidate for miniaturized and integrated devices. During the past decades, there has been remarkable progress in high-Q microresonators, including the demonstration of ultrahigh Q factors approaching a billion and Raman and Brillouin lasing. In particular, SBS, a third-order nonlinearity arising from the interaction between photon and acoustic phonon, has been shown to provide narrow linewidth, thanks to the combined effect of acoustic damping and cavity feedback. Recently, an ultra-narrow linewidth Brillouin laser has been demonstrated using a fiber resonator and also a silicon racetrack resonator, both of which operated at telecom wavelengths. A natural direction to further the current state-of-the-art is a Brillouin laser operating in the mid-infrared region. For this, chalcogenide-based microresonators make an excellent device platform and we propose narrow linewidth laser sources, based on chalcogenide microresonators.

15. SUBJECT TERMS

16. SECURITY CLASSIFICATION OF:			17. LIMITATION OF ABSTRACT	18. NUMBER OF PAGES
a. REPORT	b. ABSTRACT	c. THIS PAGE		
U	U	U	UU	22

19a. NAME OF RESPONSIBLE PERSON	19b. PHONE NUMBER *(Include area code)*
JOHN LUGINSLAND	000-0000

Standard Form 298 (Rev.5/2020)
Prescribed by ANSI Std. Z39.18

Section 2: Technical Report PDF Upload

Accomplishments

Research Objectives:

The ultimate goal of this project is to develop a narrow linewidth laser based on stimulated Brillouin scattering (SBS). Achieving narrow linewidth lasing in a portable, compact device platform is one of the outstanding challenges in the field of laser development, especially for military applications in which power, weight, size and robustness are critical. Chip-scale microresonators are the natural candidate for miniaturized and integrated devices. During the past decades, there has been remarkable progress in high-Q microresonators, including the demonstration of ultrahigh Q factors approaching a billion and Raman and Brillouin lasing. In particular, SBS, a third-order nonlinearity arising from the interaction between photon and acoustic phonon, has been shown to provide narrow linewidth, thanks to the combined effect of acoustic damping and cavity feedback. Recently, an ultra-narrow linewidth Brillouin laser has been demonstrated using a fiber resonator and also a silicon racetrack resonator, both of which operated at telecom wavelengths. A natural direction to further the current state-of-the-art is a Brillouin laser operating in the mid-infrared region. For this, chalcogenide-based microresonators make an excellent device platform and we propose narrow linewidth laser sources, based on chalcogenide microresonators.

Details of accomplishments:

1) major activities

This project has three major activities: numerical modeling, device fabrication and optical characterizations. Numerical modeling activities include device design which deals mainly with the linear optical properties of the materials and aims to identify the optimal device geometries for high Q factor. Additionally, we need to perform acoustic simulations to predict the Q factor for the acoustic modes supported by the same resonator. Then, we calculate the overlap between the optical and acoustic modes from which we can calculate the SBS gain and threshold. Fabrication also involves two different approaches: e-beam lithography (EBL) for micro-ring resonators and UV lithography for disk and wedge resonators. E-beam lithography is performed at the Center for Integrated Nanotechnology (CINT) at Sandia National Laboratory. Once the device patterns are written by EBL, the patterns are transferred to the chalcogenide device layer by inductively coupled plasma (ICP) reactive ion etching (RIE) using the in-housed RIE tool dedicated for chalcogenide device fabrication. For disk and wedge resonators, the disk patterns are defined by UV lithography and the pattern is transferred to the device layer by ICP RIE. Then, in order to obtain the desired wedge geometry, we reflow the chalcogenide layer. Finally, the fabricated devices undergo extensive optical characterizations. The first task in characterization is to determine the loss in bus waveguides and Q factors of the resonators. The losses in waveguides are measured either by cutback or overhead scattering methods. Q factors are measured from the widths of the resonance lines. By measuring the free spectral range of a

resonator, we can also determine the dispersion in the fabricated device. Once all linear characterizations are completed, we perform SBS measurements to directly determine the relevant parameters such as gain and threshold.

2) specific objectives;

The specific objective of the numerical modeling activity is to identify the device geometry including substrate and cladding that would result in the highest SBS gain and lowest threshold power. For the fabrication task, the specific objective is to be able to precisely produce a device with the prescribed geometry with lowest possible loss. For the characterization activities, the specific objectives are to perform transmission measurements with lowest possible noise and to perform SBS experiments in the most reliable way.

3) significant results or key outcomes, including major findings, developments, or conclusions (both positive and negative);

1. Design of Chalcogenide Microresonator for Stimulated Brillouin Scattering

We first built a simulation software to simulate the overlap between the acoustic and optical modes and validated it against the results in Qui et al [1]. In the process, we found a mistake in said reference which needed to be corrected to reproduce the exact gains reported. In Ref [1], suspended silicon step index waveguides are simulated for both FSBS and BSBS gain. The gain contributions are reported for the electrostriction, radiation pressure and the total gain. **Figure 1(a)** shows the reported values of each gain contribution for 4 different acoustic modes analyzed in the paper. **Figure 1(b)** shows the values generated by our simulation software, while **Figure 1(c)** shows the ratio of the values produced in our simulation divided by those in Ref. [1]. To produce the same values as those in the paper we had to make two primary changes in our code. This was to the radiation pressure calculation and the electrostriction calculation.

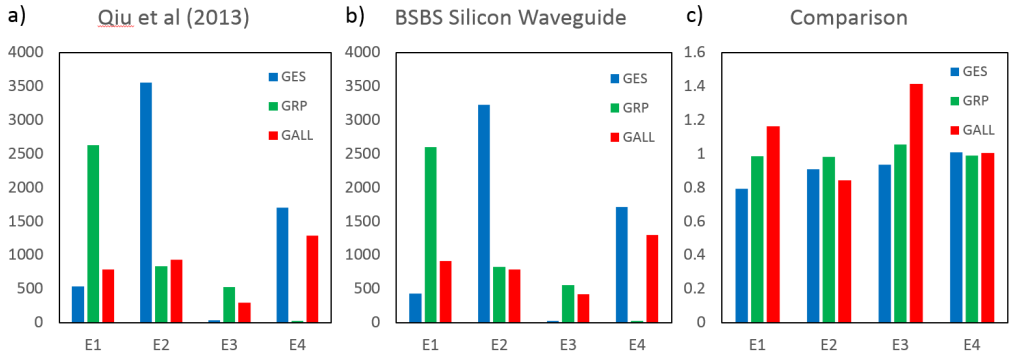

Figure 1. Simulated BSBS gain for a suspended silicon waveguide and the reported BSBS gain from Qui et al (2013) [1], in units of $m^{-1}W^{-1}$. (a) The reported values of BSBS gain reproduced from Qui et al. (b) Values produced from our simulation after fixing the radiation pressure and electrostriction boundary force. These values include the approximation that the group index and material index are the same. (c) A comparison of our simulation and Qui et al. generated by dividing the values we obtain by the values reported. A perfect agreement would then correspond to a value of 1.

The radiation pressure calculation had an issue with the continuity of the boundary of the exported simulations from COMSOL. The boundaries are exported as a series of points whose order does not necessary correspond to a continuous curve. This results in discontinuities in the radiation pressure overlap integral. To prevent this, we created a function which post processes the boundary of the simulated geometry to create a continuous curve. The second issue that we found in our code was that the boundary electrostriction force was consistently twice as low as those reported in Qui et al [1]. We determined that this was due to using a second order difference methods to calculate derivatives during the optical force calculation. The second order difference caused the boundary optical force to be spread over two cells, while the acoustic boundary force, which requires no derivatives to calculate, occurs in only one. To fix this we used a first order difference method which prevents this boundary duplication but also reduces the size of the simulation area by 1 along each axis. The acoustic force matrices then had to also be contracted by 1 along each axis to allow for matrix multiplication to be valid. This was done by taking the maximum of the field between each point. While this makes our simulation more accurate, it also makes it more dependent on a finer mesh for proper convergence. Lastly, we found that in the report by Qui et al., every instance of the group index (1.8) was simply approximated by the refractive index of silicon (3.5) which resulted in a change of the gain by about factor of 4.

Using our newly revised code, we resimulated the gain for the various types of resonator devices we have been fabricating out of $Ge_{23}Sb_7S_{70}$ (GeSbS) and $Ge_{28}Sb_{12}Se_{60}$ (GeSbSe). This year, we have begun the fabrication and optimization of GeSbS waveguides and ring resonators using the same fabrication process we have used for GeSbSe [2]. In our most recent iteration of the fabrication process, we have fabricated waveguides 980 nm tall by 780 nm wide which support multiple optical modes. This multi-mode behavior allows for intermodal SBS, where an optical photon is scattered between two different waveguide modes. Intermodal SBS has the benefit of allowing smaller resonators as the free spectral range (FSR) is not limited by the SBS shift. **Figure 2(a)** shows the optical force generated in this waveguide when pump and Stokes mode are the fundamental TE and second order TE modes, respectively. This force profile has a high overlap with the acoustic mode shown in **Figure 2(b)**. This is primarily due to the bulk electrostriction gain. The total gain of this interaction is 512 $m^{-1}W^{-1}$.

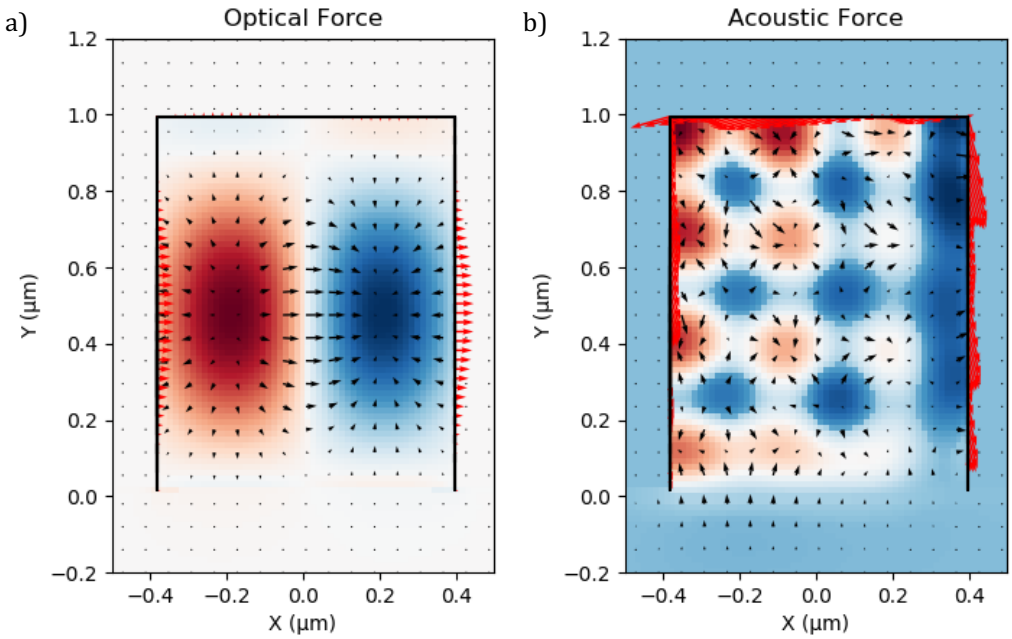

Figure 2. (a) A plot of the simulated optical force due to a BSBS interaction between the fundamental TE and second order TE modes. The black line depicts the boundary of the waveguide. The red and blue color depicts the intensity of the longitudinal optical force while the black vector field depicts the transverse components. The red arrows at the boundary depict the radiation pressure. (b) A plot of the acoustic mode with the highest overlap with the optical force shown in (a). The acoustic mode is confined to the chalcogenide waveguide with little leakage into the SiO_2 substrate due to the large sound velocity mismatch. This acoustic mode has a frequency of 6.48 GHz and the gain is 512 $m^{-1}W^{-1}$.

Currently we can fabricate GeSbS wedge resonator on a SiO_2 substrate with high Q factor. These geometries were simulated to determine the configurations with highest gain. **Figure 3(a,b)** show the maximum gain configuration for a 21° wedge that is 3.4 μm thick and is attached to a SiO_2 substrate. The tip of the resonator is rounded in simulation to prevent divergences in the acoustic mode simulation. The resulting gain is 14 $m^{-1}W^{-1}$ which is higher than the previous report due to the increased boundary electrostriction force.

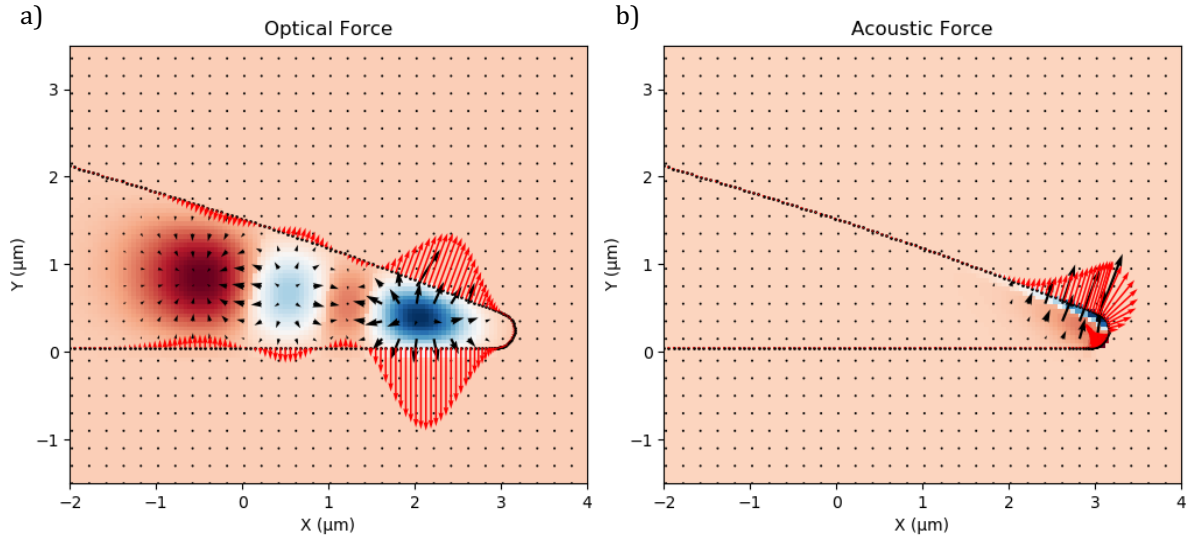

Figure 3. (a) A plot of the simulated optical force due to a BSBS interaction between the fundamental TE and third order TE mode. The black line depicts the boundary of the wedge. The components of the plot are described in Figure 1. The wedge angle is 21 degrees. (b) A plot of the acoustic mode with the highest overlap with the optical force shown in (a). This wedge is on a silica substrate which prevents boundary forces on the lower boundary. This acoustic mode has a frequency of 3.74 GHz and the gain is 14 $m^{-1}W^{-1}$.

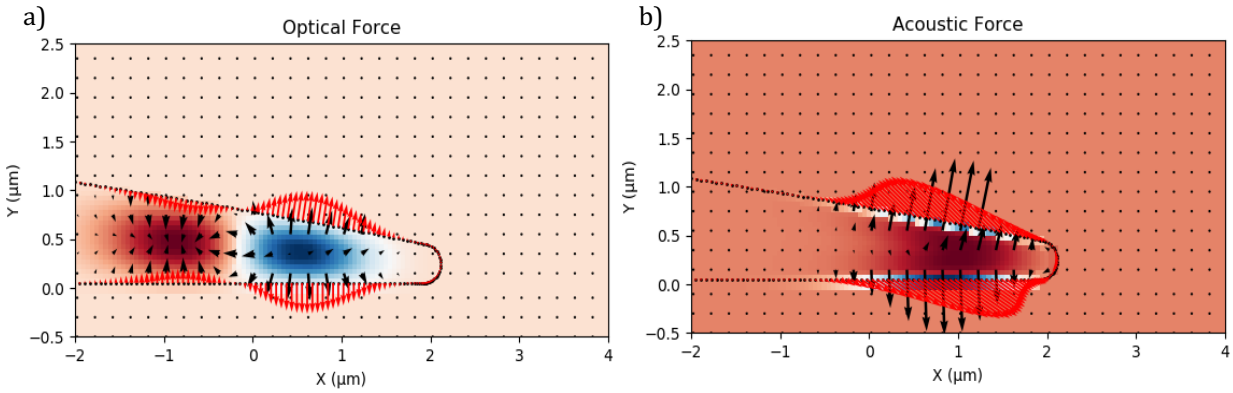

Figure 4. (a) A plot of the simulated optical force due to a BSBS interaction between the fundamental TE and second order TE mode. The black line depicts the boundary of the waveguide. The components of the plot are described in Figure 1. The wedge angle is 11 degrees. (b) A plot of the acoustic mode with the highest overlap with the optical force shown in (a). In this device the wedge is undercut this will result in a higher acoustic Q factor and also increases the total boundary forces. This acoustic mode has a frequency of 3.83 GHz and the gain is 34 $m^{-1}W^{-1}$. However, the acoustic Q could be as high as 10^4 resulting in 340 $m^{-1}W^{-1}$.

Using the update code, we additionally simulated what changes to the geometry could increase the gain and acousto-optic overlap. We found that in general decreasing the radius of the resonator or decreasing the wedge angle results in a high BSBS gain. This is due to the increased

overlap of the optical and acoustic modes with the boundary of the resonator. Additionally, undercutting the resonator increased the gain by a factor of 2 by freeing the lower surface to vibrate and thus to contribute to gain. The optimized version of the wedge resonator gain is shown in **Figure 4 (a,b)**. This design has an acoustic gain of 34 $m^{-1}W^{-1}$. Freeing the resonator to vibrate should also increase the acoustic Q factor of the resonator which may be as high as 10^4 which is 10 times large than the bulk value of 10^3. This would result in a gain of 340 $m^{-1}W^{-1}$ which would lead to micro-watt level thresholds.

Simulations were also performed for the 21° undercut wedge resonator for FSBS. In FSBS, the pump and Stokes waves are co-propagating instead of counter-propagating. The momentum of the acoustic mode is zero i.e. a standing wave. The highest gain occurs for the fundamental mode and an acoustic mode at 270 MHz with a gain of 2.5×10^6 $m^{-1}W^{-1}$, which is higher than that of an As_2S_3 sphere, but is at a much higher frequency. A lower frequency acoustic mode may be required to stay within the band of the optical resonance. A resonance at 6.6 MHz showed a gain of 2.5×10^5 $m^{-1}W^{-1}$.

2. Fabrication of Chalcogenide Microresonator

2.1 Fabrication of reflowed wedge resonator

We developed a new fabrication process for the chalcogenide rounded-wedge resonators by using a negative photoresist. As shown in **Figure 5**, the resonators were fabricated by the standard photolithography process followed by two thermal reflow processes, first on the photoresist disk and then on the chalcogenide wedge disk. Previously, we were using a positive photoresist (AZ P4210) to create an etch mask for chalcogenide wet etching. However, the photoresist's developer was a potassium-based alkaline solution that dissolves chalcogenide glasses. Thus, the chalcogenide wet etching started during the photoresist development process, giving us no chance to improve the photoresist disk's edge roughness before the chalcogenide wet etching.

Switching to a negative photoresist (NR9-1000P) allowed us to improve the edge roughness of our resonators in two ways. First, the developer for NR9-1000P did not dissolve the chalcogenide glass and thus the wet etching process can be controlled better. Additionally, we could add a photoresist reflow process to significantly reduce the edge roughness of the photoresist disk. As shown in the third step of **Figure 5,** the photoresist disk was reflowed at 150 °C for 2 min to achieve an ultrasmooth edge as shown in the scanning electron microscopy (SEM) image (**Figure 6a**). A smooth photoresist edge is extremely important for our fabrication as it directly determines the edge roughness of the chemically etched chalcogenide wedge, which further determines the edge roughness of the undercut silica pillar as well as the finally reflowed rounded-wedge resonator. **Figure 6(b,c)** further confirm that the chalcogenide wedge etched with a reflowed photoresist mask has a much smoother edge and less wrinkled top surface.

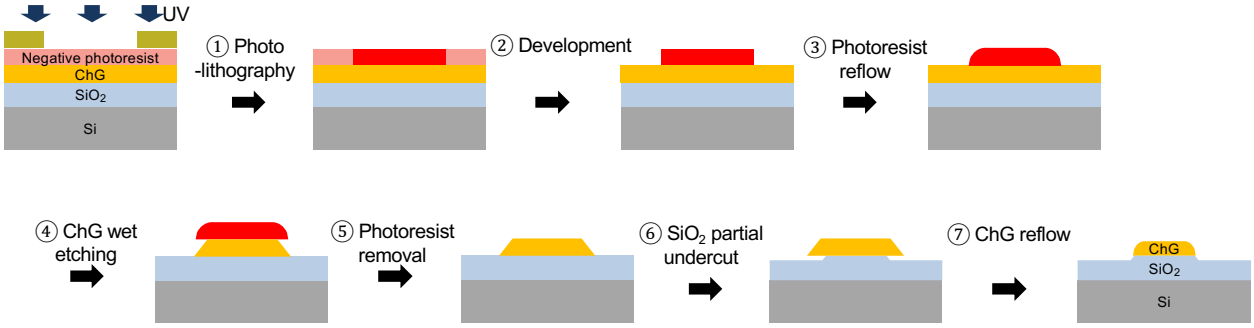

Figure 5. The new fabrication processes of the $Ge_{23}Sb_7S_{70}$ chalcogenide (ChG) rounded-wedge resonator with a negative photoresist (NR9-1000P). First, a 3.9-µm-thick $Ge_{23}Sb_7S_{70}$ glass was thermally evaporated on a 6-µm-thick silicon dioxide substrate. Then, we spin-coated the photoresist on top of the chalcogenide layer and patterned microdisks with a diameter of 160 µm. The developer for the negative photoresist doesn't dissolve ChG, and thus, the photoresist disk can be achieved without damaging the ChG. The reflow process makes the edge of the photoresist smoother, resulting in the smooth ChG wedge disk after the wet etching. Then a 0.5-µm-deep silicon dioxide partially undercut was created through SiO_2 wet etching. Finally, the chalcogenide wedge resonator itself was reflowed to further smooth the surface and obtain rounded-wedge profile needed for high quality factor.

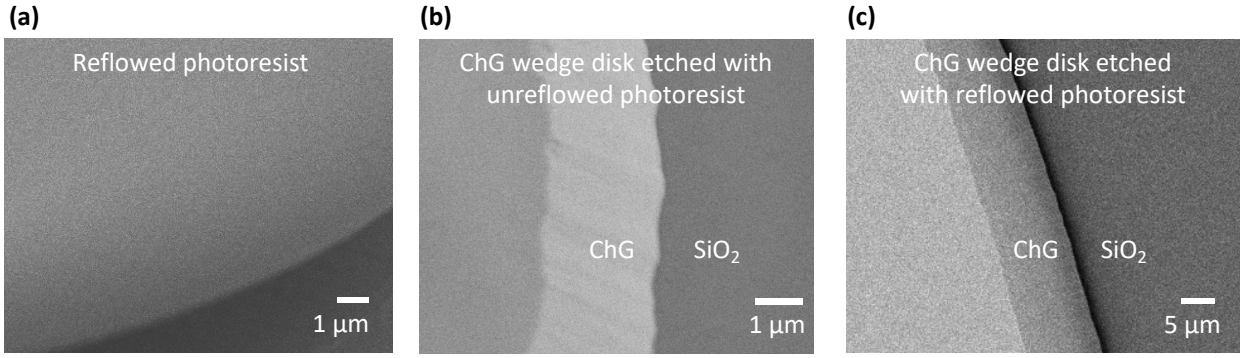

Figure 6. SEM images of photoresists and chalcogenide wedge disks before the chalcogenide reflow process. (a) SEM image of the reflowed photoresist disk on ChG glass. (d) SEM image of a ChG wedge disk after the wet etching process with an unreflowed photoresist mask. (e) SEM image of a ChG wedge disk after the wet etching process with a reflowed photoresist mask. The edge profile of the ChG wedge disk etched with a reflowed photoresist is significantly smoother than the unreflowed case.

Before finally reflowing the chalcogenide disks, we partially etched the silicon dioxide substrate to create an overhang which prevents the formation of cracks due to thermal stress on chalcogenide glass during the reflow process. Then we reflowed the chalcogenide disks at 475 °C to achieve a very smooth wedge-profile with varying angles depending on the reflow time, as reported last year. We characterized the rounded wedge resonators to quantify the surface

roughness which directly impacts the quality factor. As shown in **Figure 7**, atomic force microscopy (AFM) scans confirmed that the reflow process not only changes the wedge profile but also decreases the surface roughness dramatically. We used large (800 – 900 μm in diameter) resonators so that the AFM scan can be performed more easily. As the reflow time is increased, the chalcogenide microdisk's wedge angle becomes smaller, as shown in **Figure 7(a-c)**. The unreflowed chalcogenide wedge in **Figure 7d** has a surface roughness of 9.8 nm, which is created by the wet etching process. The surface roughness decreases to 0.2 nm by reflow in **Figure 7(e-f)** thanks to the smoothing effect of surface tension on the slightly melted chalcogenide glass.

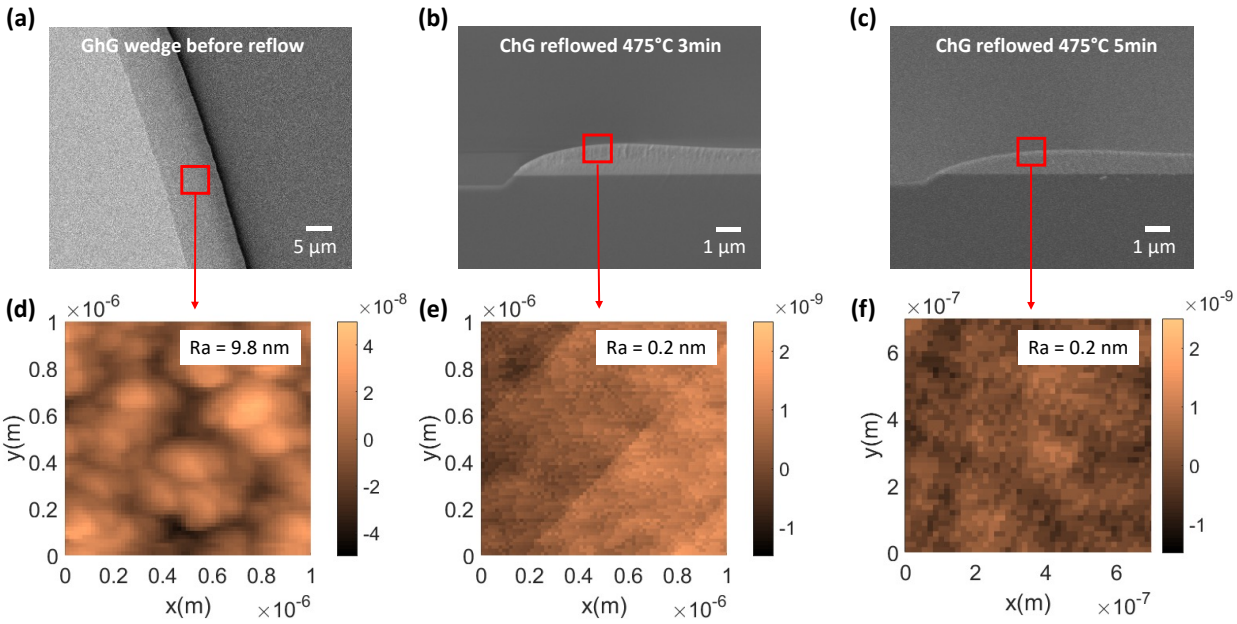

Figure 7. Images of chalcogenide wedge disks before and after the ChG reflow process. (a-c) SEM images and (d-f) AFM measurement of rounded wedge disks with the reflow time of 0 (as prepared), 3 and 5 min at 475°C, respectively.

2.2 Dispersion control of $Ge_{23}Sb_7S_{70}$ reflowed wedge resonators

We further investigated the optical mode geometry and dispersion engineering of our reflowed sulfide wedge resonators for intermodal SBS generation. In general, the fundamental optical mode of a thick wedge resonator is difficult to access due to its weak overlapped with the wedge top surface. Also, a thick reflowed wedge profile cannot provide significant confinement of the fundamental modes, resulting in the mode migration towards smaller effective radius at long wavelengths that leads to a large normal dispersion. Thus, we significantly reduced the thickness of our wedge disks to promote tapered fiber coupling with the fundamental mode and low radial order modes used for intermodal SBS generation. And to stop the fundamental mode from migrating inwards, we proposed to "trap" them in the reflowed wedge curves around the mode profile as shown in **Figure 8(a)**. Fabrication wise, this kind of reflowed wedge profile can be achieved with a sub-wavelength sulfide disk thickness and a short reflow time.

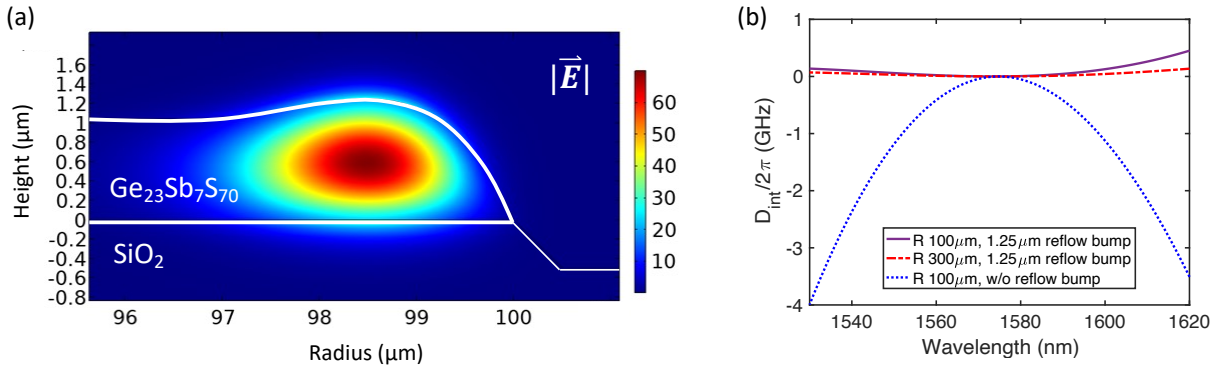

Figure 8. (a) The cross-section of a dispersion engineered thin sulfide reflowed wedge with 100 μm-radius, 1 μm disk thickness, 1.25 μm reflow bump height and its TE_{00} mode profile. (b) Simulated TE_{00} mode integral dispersion D_{int} of sulfide reflowed wedges with 1.25 μm reflow bump height and different radiuses compared to a not reflowed sulfide disk which has large normal dispersion. By tuning the radius dimension, we can optimize the geometry dispersion slope and flatten the total dispersion curve.

The volume of displaced sulfide during the reflow process is determined by the non-reflowed sulfide disk's radius, thickness, and its silica substrate's partial undercut depth. This allowed us to deterministically calculate and engineer a reflowed wedge profile with any combination of thickness, radius, and reflowed bump height by tuning the reflowed bump width which is determined by reflow time. We simulated the fundamental TE mode's dispersion of wedges with different reflowed bump width and found that a few-microns-wide reflowed bump can provide a tighter radius confinement of the resonator's TE_{00} mode and push its dispersion into the anomalous region. This proved that our geometry design can overcome large normal material dispersion and tightly confine the optical mode to the tip of the wedge geometry which benefit the mode overlap with acoustic modes. We can further tune the other parameters, such as the radius of the resonator to flatten the total dispersion curve as shown in **Figure 8(b)**, which allows stabilization of the optical mode location over large bandwidth.

Dispersion controlled sulfide reflowed wedge resonators were fabricated through a combination of photolithography, wet-etching and thermal reflow. Briefly, a sulfide thin film was first evaporated onto a silicon substrate with a 6 μm thick thermal oxide. A photoresist (NR9-1000PY) pattern was then defined by the standard photolithography process. Then, the photoresist pattern was reflowed at 130 °C to minimize the edge roughness. With this pattern, the sulfide layer was etched in controlled KOH water solution flow to produce a sulfide disk with 90° sidewall angle. Next, the sulfide disk is soaking in buffered oxide etch (BOE) to create a partial undercut on its silica substrate which defines the radius of the reflowed wedge. Lastly, sulfide reflow process is conducted to produce the designed reflowed bump. As shown in **Figure 9(a),** by sweeping the reflow temperature and time we were able to create a reflowed bump profile very close to the optimized design. By giving the tapered As_2S_3 fiber a negative surface charge using an anti-static gun, we can reliably control the fiber's coupling point on the reflowed bumps and get full-band transmission spectrum of the TE_{00} mode. By Lorentzian fitting each resonance, we extracted the integral dispersion spectrum of the reflowed wedge resonator that

clearly shows a flat anomalous dispersion compared to a not reflowed sulfide disk with large normal dispersion, as shown in **Figure 9(b)**.

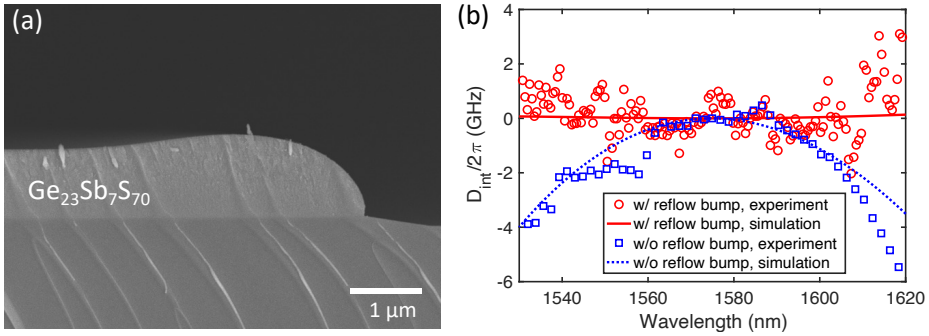

Figure 9. (a) Cross-section SEM image of a fabricated sulfide reflowed wedge resonator with 300 μm-radius, 0.95 μm-disk thickness and 1.23 μm reflow bump height. (b) The integral dispersion (D_{int}) spectrum of the reflowed wedge resonator clearly shows a flattened dispersion compared to a sulfide disk without reflow bump, matching well with simulation.

However, we also observed a lot of small particle residues on top of the fabricated reflow wedges, as shown in **Figure 10(a)**, which limited the quality factors of these wedge resonators to 3×10^4. Judging by the fact that these particles were not dissolved in water rinse nor reflowed with sulfide, they were likely GeS_2 particles separated from the sulfide glass network during the BOE etch and left on the surface. To improve BOE etch process, we made a dual layer Teflon beaker that introduces a slow etchant flow around the upward-facing sulfide chip during the BOE wet etch. The stirring flow can quickly bring any kind of etch byproducts away and we clearly observed the elimination of the small particle residues from the stirless BOE wet etch. As shown in **Figure 10(b)**, the reflowed wedge fabricated with stirring BOE shows clean top surface of the reflowed edge which led to an intrinsic quality factor of 1.0×10^5 that is 3 times higher than wedges fabricated with stirless BOE wet etch [**Figure 10(c)**]. We plan to fabricate more reflowed wedges with various radiuses and find the average Q of our improved fabrication process.

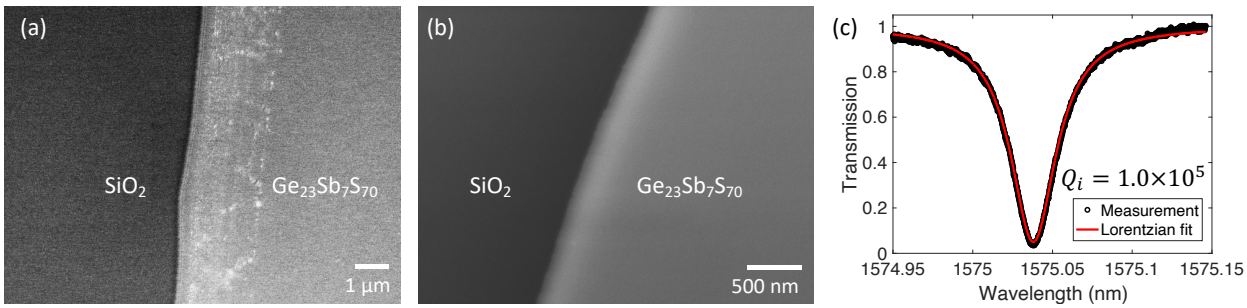

Figure 10. Top-view SEM images of the reflowed edge of a sulfide wedge resonator fabricated using (a) stirless BOE wet etch and (b) stirring BOE wet etch. There are a lot of small particle residuals on top of the reflow bump in (a) but no small particle clusters or reflow nonuniformity

was observed on (b). (c) Transmission spectrum of a TM_{00} mode resonance of a 150 μm-radius sulfide wedge resonator fabricated using stirring BOE wet etch. The wedge is close to critical coupled around 1575 nm wavelength and has an intrinsic Q of 1.0×10^5.

2.3 Fabrication of $Ge_{23}Sb_7S_{70}$ waveguides and ring resonators

In order to improve the Q factor and SBS gain, we focused on $Ge_{23}Sb_7S_{70}$ (sulfide) material and large cross-section multimode waveguide geometry. We first targeted optimizing the e-beam lithography (EBL) conditions, systematically investigating EBL resist exposure dose optimization, multi-pass EBL averaging effects and reflow of the EBL resist. For exposure dose optimization, instead of optimizing the resist sidewall angle and corner sharpness after development, we used the line edge roughness of etched sulfide waveguides as the optimization criterion and found the best exposure dose to be 320 μC/cm^2, which is 15% higher than the dose we used for previous fabrications. As shown in **Figure 11**, using the optimized exposure dose significantly reduces the line edge roughness of etched sulfide waveguides to 1.1 nm which was comparable to the state-of-the-art silicon devices.

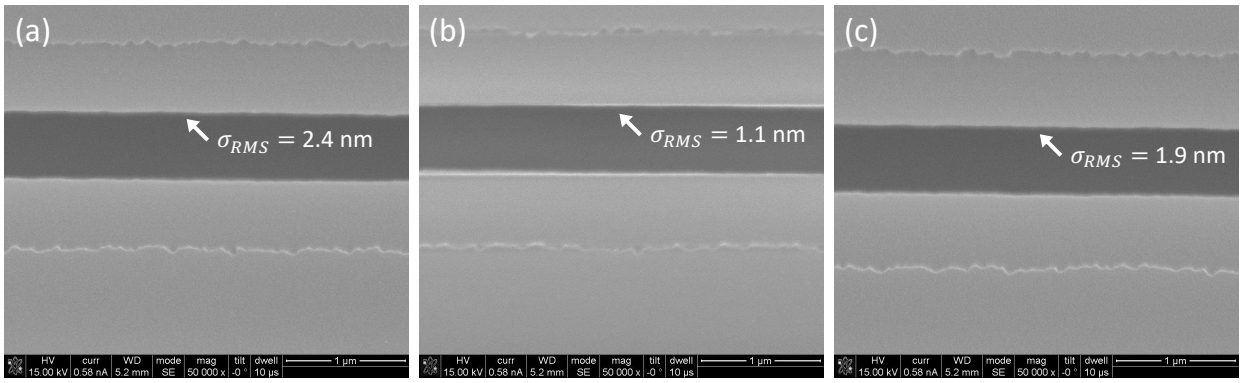

Figure 11. SEM images of sulfide waveguides etched using EBL patterns written with exposure dose of (a) 300 μC/cm^2, (b) 320 μC/cm^2 and (c) 340 μC/cm^2. The line edge roughness was measured to be 2.4 nm, 1.1 nm, and 1.9 nm, respectively. The beam current spot size was 7.54 nm, and the shot pitch was 6 nm. With such beam condition, the EBL exposure dose optimized for sulfide dry etch is 320 μC/cm^2.

For multi-pass EBL, we did not observe either line edge roughness improvement or ring resonator Q factor improvement compared to the single-pass EBL devices. For EBL resist reflow, we investigated reflow temperature from 120°C to 150°C and did not observe obvious line edge roughness improvement on the etched sulfide waveguides. We then reflowed the EBL pattern on a chip from this January at 140°C and observed a decrease in etched ring resonator Q factors, which is likely due to etch punch-through at the thinned resist edges. To conclude, using single-pass EBL with 320 μC/cm^2 exposure dose without reflow is our optimized EBL process. We then established and optimized the inductively coupled plasma - reactive ion etching (ICP-RIE) process of sulfide and successfully fabricated on-chip sulfide ring resonators with intrinsic quality factors up to 6×10^5. After a comprehensive study of every parameter in the etch recipe, we found that Cl_2 prohibits the formation of passivation layers during sulfide dry etch

consequently resulting in rough sidewalls. Thus, we employed Cl_2-free etch chemistry with 1:1 flow rate ratio of BCl_3/Ar and further optimized the chamber pressure to achieve smooth and vertical the sidewalls as shown in **Figure 12(a).** Using the optimized etch recipe, we fabricated single-mode rings with cross-sectional dimensions of 420 × 750 nm and achieved intrinsic Q factors of 2.0×10^5 for its TE_{00} mode, indicating single mode waveguide loss of 1.9 dB/cm. We then fabricated multi-mode rings with larger cross-sectional dimensions of 600 × 1600 nm, as shown in **Figure 12(b)**, for which concentric Pulley couplers were designed to selectively couple with the TE_{00} mode and filter out the lossy higher order modes. The multi-mode rings exhibited an improved intrinsic Q factor of 6.0×10^5 for its TE_{00} mode [**Figure 12(c)**], indicating a significant improvement of waveguide loss to 0.64 dB/cm when using a large cross-section geometry.

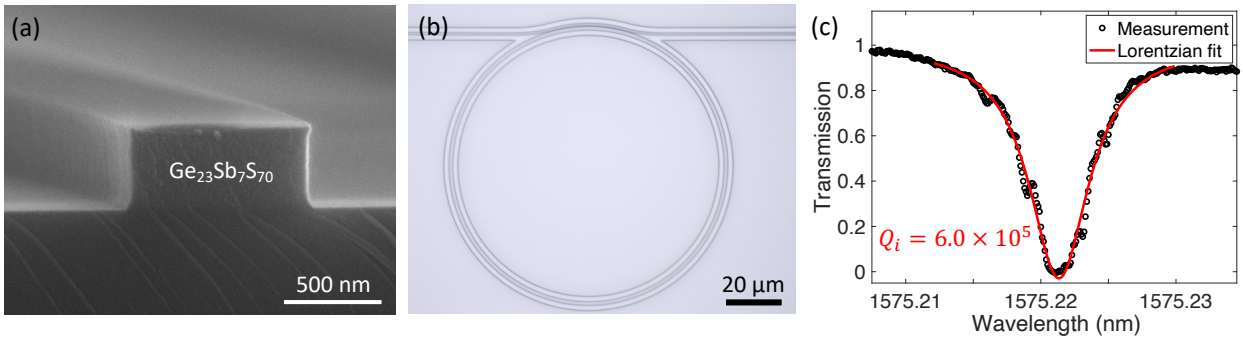

Figure 12. (a) SEM image of a sulfide waveguide. (b) Optical microscopic image of a 50 µm-radius sulfide multi-mode ring resonator and its single mode bus waveguide fabricated by EBL and ICP RIE using chlorine chemistry. (c) Transmission spectrum of a multimode ring resonator exhibiting $Q = 6 \times 10^5$ near $\lambda = 1575$ nm.

2.4 Optical characterizations of wedge resonators

We used a tapered As_2S_3 chalcogenide fiber to couple light into the rounded-wedge resonators for optical characterizations. As shown in **Figure 13(a)**, we used a silica lensed fiber to focus the input light from a single frequency mode-hope-free tunable CW laser in 1550 nm band into the tapered As_2S_3 fiber with 30% coupling efficiency. The As_2S_3 fiber tapering condition was tuned by changing the pulling length, duration, and speed to achieve a waist diameter of around 0.8 µm as shown in **Figure 13(b)**, which has an effective index of 2.1. The resonators were fabricated at a corner of the substrate to avoid any interference from the substrate and mounted on a 5-axis stage with build-in piezo-controllers to optimize coupling conditions with the tapered fiber as shown in **Figure 13(c)**.

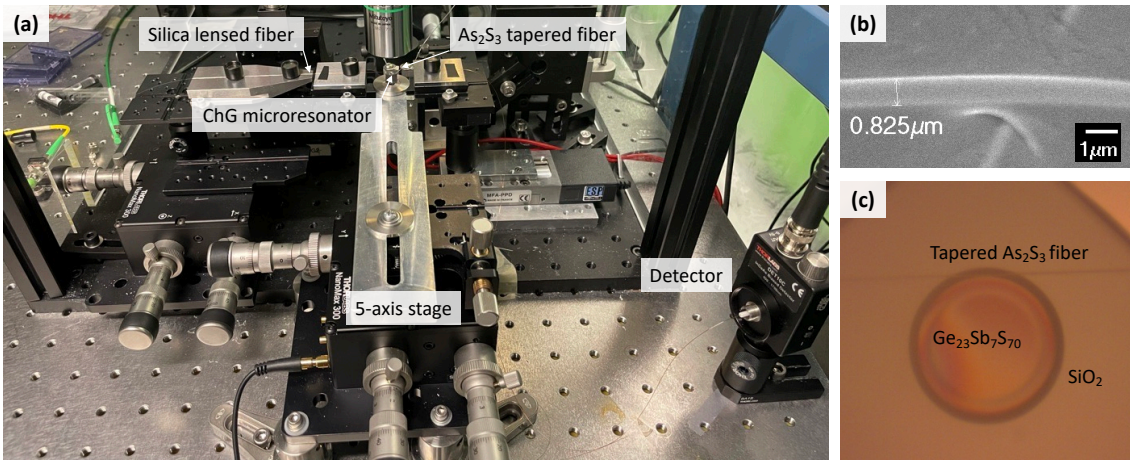

Figure 13. Images of chalcogenide rounded-wedge resonator measurement set-up. (a) Photo of the As_2S_3 tapered fiber coupling system. (b) SEM image of the tapered waist of the As_2S_3 fiber. (c) Optical microscope image of a round-wedge resonator with diameter of 160 μm coupled to a tapered As_2S_3 fiber.

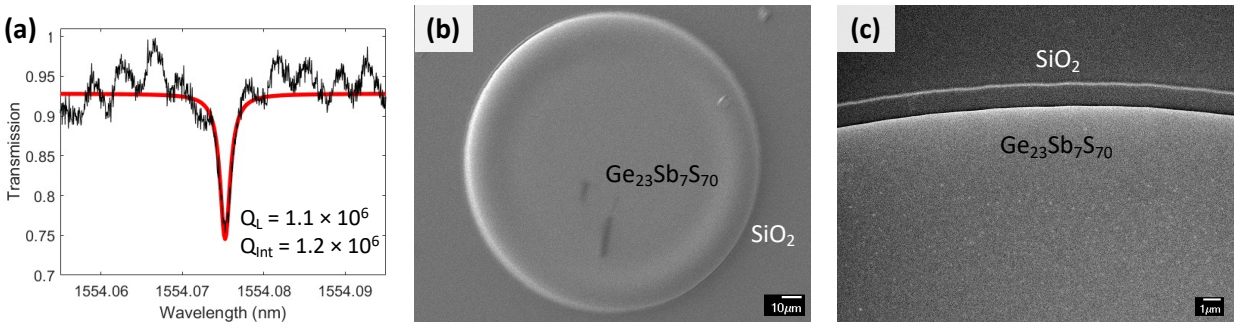

Figure 14. (a) Transmission spectrum of a 160-μm-diameter round-wedge resonator measured by a CW tunable laser. The wavelength is around 1554 nm with input power around 1 μW. The red curve is a Lorentzian fit of the mode. (b-c) SEM images of the high-quality round-wedge resonator. The top surface is smoothed by the thermal reflow while the edge roughness is still limited by the wet etching uniformity.

The optical transmission of the rounded wedge resonators was measured by a photodetector and an oscilloscope while the laser was scanned continuously with a scan rate of 0.5 nm/s. The transmission dip was fit with a Lorentzian lineshape function and a loaded quality factor of $Q_L = 1.1 \times 10^6$ and an intrinsic quality factor of $Q_{Int} = 1.2 \times 10^6$ were measured as shown in **Figure 14(a)**. At this time, we employed a polymer (Poly(methyl methacrylate)) coating on top of the resonator both to prevent damage and to avoid any contamination from the environment. Additionally, the polymer coating acted as a spacer layer between the fiber and the resonator to achieve a critical coupling condition. The SEM images [**Figure 14(b-c)**] of the high-quality round-wedge resonator further evidenced both surface and edge roughness improvement from our new fabrication process that enabled us to achieve this order of quality factor on chalcogenide microresonators.

2.5 Forward Stimulated Brillouin Scattering Measurements

We examined the possibility of forward SBS in chalcogenide microresonators. The results from the following section have been published in [3]. We were inspired to explore this avenue by the fact that the expression for the Brillouin gain G_m is inversely proportional to the square of the frequency of the acoustic mode (same as the Brillouin shift)

$$G_m = \frac{2\omega Q_m}{\Omega_m^2 v_{gp} v_{gs}} \frac{|\langle \mathbf{f}, \mathbf{u}_m \rangle|^2}{\langle \mathbf{E}_p, \varepsilon \mathbf{E}_p \rangle \langle \mathbf{E}_s, \varepsilon \mathbf{E}_s \rangle \langle \mathbf{u}_m, \rho \mathbf{u}_m \rangle}. \quad (1)$$

where Ω_m is the acoustic frequency. Since the momentum of the phonon is the difference of the momenta of the pump and Stokes photons in the case of forward SBS (as opposed to the sum of the momenta of the two photons in the case of backward SBS), we expect the phonon frequency in resonant microcavities to generally be much smaller than in BSBS. Our simulations indicated that acoustic frequency for BSBS should be around 7 GHz while acoustic frequency for FSBS should be closer to tens of MHz.

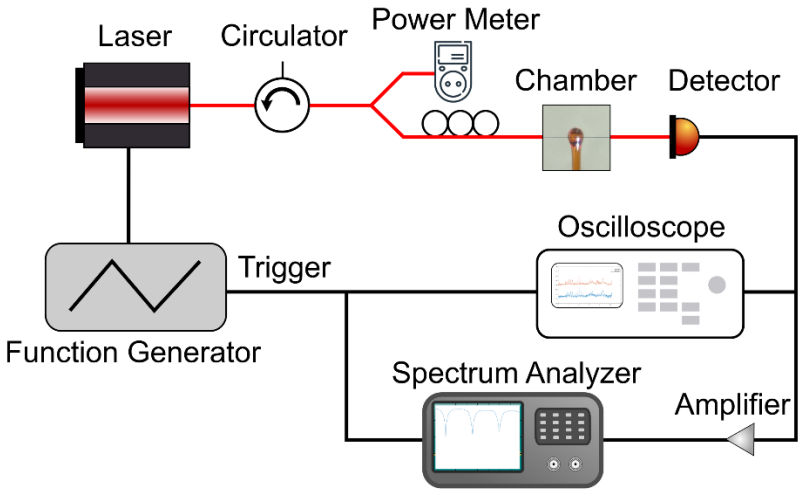

Figure 15. Experimental setup for measuring forward Brillouin scattering in microresonators. We used a tunable diode laser at 1550 nm as the pump. We used a power splitter to reduce the pump power to avoid thermal effects while operating the laser above the threshold. The laser was coupled into the resonator via a tapered silica fiber. The Stokes beam from the resonator was coupled back into the tapered fiber.

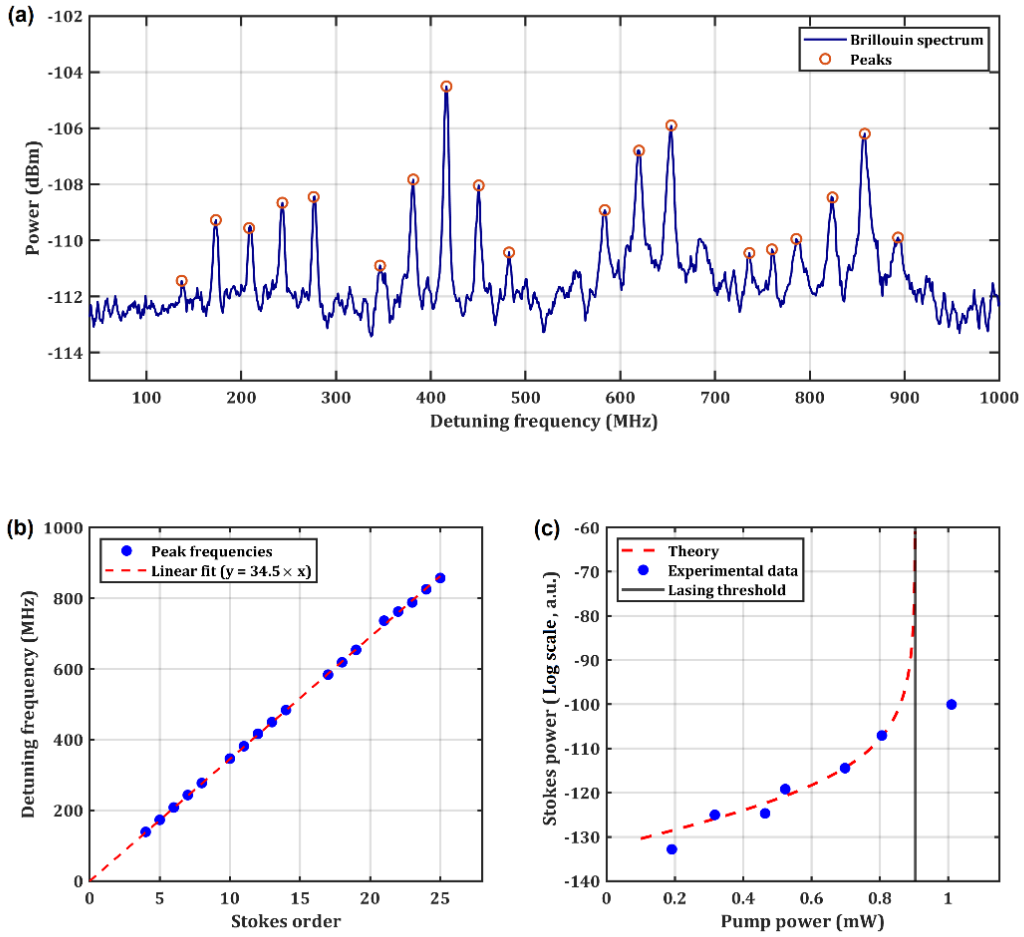

Figure 16. (a) Cascaded FSBS spectrum in a 125 µm sphere with an unloaded quality factor 1 x 10^6. The x-axis is the detuning from the pump and the y-axis on the left shows the power of the beat note. This measurement was taken in the overcoupled regime using a 1.2 GHz bandwidth detector and the spectrum was averaged over 41 sweeps. The red circles highlight the location of the peaks in the spectrum. (b) The frequency shifts of the Stokes beams from the pump, which are observed to be integer multiples of 34.5 MHz. The acoustic mode simulated in **Fig. 4** agrees well with the observed FSBS shift. (c) The power of the first Stokes beam vs. pump power for a 110 µm resonator of Q factor 2.2 x 10^6 showing an FSBS shift at 18.3 MHz. The experimental data is fit to the small signal approximation (SSA) model [4]. The SSA model is valid only below the Brillouin lasing threshold - therefore, the one data point above the threshold was not fit to the model. The SSA model breaks down at the threshold shown by the vertical black line, and goes to infinity. The stimulated lasing threshold was found to be 900 ± 20 µW, beyond which cascaded Stokes beams were observed.

The experimental setup is shown in **Figure 15**. An SMF-28 silica fiber was tapered to 500 nm radius by heating the fiber to above the glass transition temperature using a butane flame while stretching the fiber from both ends using motorized stages. The laser source was a single frequency mode-hop-free tunable CW laser in a 1550 nm band (Toptica CTL 1550). The resonator was mounted on a 3-axis piezo-actuated stage (Thorlabs MAX312D) with 20 nm resolution and brought within 100 nm of the tapered fiber. The system was imaged using a microscope with a long-distance objective from the top. The system was enclosed in a chamber to minimize disturbances due to temperature fluctuations and air currents. The transmitted light was measured using an InGaAs photodetector of 1.2 GHz bandwidth (Thorlabs DET01CFC) for the spectrum in **Figure 16(a)** and an InGaAs photodetector of 40 MHz bandwidth (Thorlabs DET10C) for the spectrum in **Figure 17**. A 20 dB amplifier was used with the high-bandwidth detector to make up for the lower responsivity. The signal was recorded using an oscilloscope and an RF spectrum analyzer (Keysight N9030B). A function generator provided a triangle wave signal to the laser to sweep the frequency by a few tens of GHz, and a trigger signal to the RF spectrum analyzer and the oscilloscope. The laser was tuned into resonance by scanning for the characteristic dip in transmission across the tapered fiber on the oscilloscope. The Stokes beams in the resonator are coupled back into the tapered fiber. The electrical spectrum analyzer was used to pick up beat notes between the Stokes beams and the pump that are typically too close for an optical spectrum analyzer to resolve. Using this setup, we observed the cascaded Brillouin spectrum shown in **Figure 16(a)** from a 125 µm resonator of unloaded quality factor 1 x10^6 and the spectrum in **Figure 17** from a 100 µm resonator of unloaded quality factor 6.2 x 10^5. The FSBS shift agrees well with the simulation (**Figure 18**).

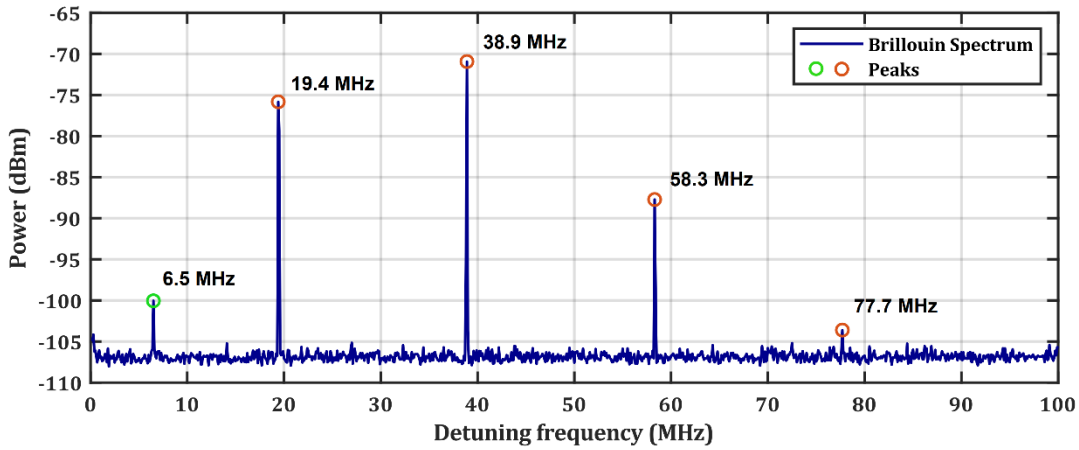

Figure 17. Cascaded FSBS spectrum in a 100 µm sphere with unloaded quality factor 6.2 x 10^5. We did not use an amplifier for this measurement and time averaging was not necessary. The spectrum was taken using a detector of high responsivity and 40 MHz typical bandwidth. The peaks highlighted in red are part of the cascaded spectrum, with a Brillouin shift of 19.4 MHz. The 6.5 MHz peak results from an acoustic mode having a weaker overlap with the pump and therefore does not cascade. The pump was blue-detuned from the resonance, hence the 19.4 MHz peak experiences more loss than the 38.9 MHz peak. The number of Stokes orders observed is

likely bandwidth-limited by the detector. The linewidth of the Stokes beams is less than the frequency resolution at 100 kHz.

To estimate the lasing threshold, we used a microsphere of diameter 110 μm with quality factor 2.2 x 10^6, showing cascaded Stokes beams separated by 18.3 MHz. As the pump power was reduced, the first Stokes line was the last to drop below the noise floor of the spectrum analyzer. We then slowly ramped up the pump power and recorded the power of the first Stokes line until we observed cascaded comb lines again.

Finite element simulations of this sphere revealed a resonant acoustic mode at 16.1 MHz that satisfies the phase matching condition, close to the observed FSBS shift at 18.3 MHz. Using **Eq. (1),** we estimated the Brillouin gain Γ of the resonator to be 5.14 x 10^5 $m^{-1}W^{-1}$. The calculated value of Γ was used to fit the theoretical model in [4] to the experimental data to obtain the coupling constant τ and the threshold power. The small signal approximation breaks down at the Brillouin lasing regime and the theoretical model goes to infinity at the threshold (**Figure 16(c)**). From the fit, we found the Brillouin lasing threshold to be at 900 ± 20 μW, for coupling constant τ = 0.85. Beyond the threshold, cascaded Stokes beams were observed. The lasing threshold was experimentally observed to be in a similar range for all spheres with a Q-factor around 10^6 with comparable coupling conditions.

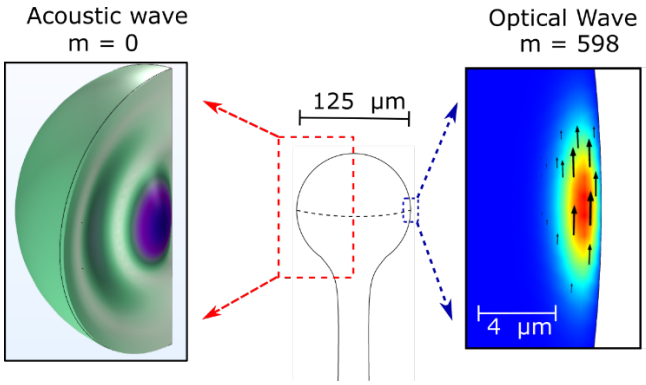

Figure 18. Simulations of optical and acoustic modes for phase-matched Brillouin scattering in an As_2S_3 microsphere of diameter 125 μm. The acoustic eigenmode oscillating at 33.2 MHz is shown on the left. Purple highlights the region with the highest deformation. Deformation is exaggerated to show the effect. The electric fields to the right correspond to optical excitation at 1550 nm with the azimuthal mode order represented by m. The colors show the strength of the electric field, and the arrows show the electric field direction.

Previous theoretical work has established that anti-Stokes beams will be generated along with Stokes beams in a waveguide beyond the threshold for cascaded forward Brillouin scattering [5]. The analysis also applies to resonators that are simultaneously resonant for the pump, Stokes, anti-Stokes and acoustic waves. However, a direct measurement of the beat note between the pump and the anti-Stokes beams does not allow an independent measurement of the anti-Stokes beams. This is because the beat note between the pump and the anti-Stokes beam has the same frequency as the beat note between the pump and the Stokes beam and the latter

eclipses the signal from the anti-Stokes beam, as Stokes beams are stronger than anti-Stokes beams. It is also not easy to resolve the Stokes and anti-Stokes beams using an optical spectrum analyzer since they are separated by less than 100 MHz. Therefore, it is necessary to perform a heterodyne measurement with a probe laser at a frequency different from the pump beam to ensure the Stokes and anti-Stokes beams are mapped to unique beat frequencies. The schematic for this measurement is shown in **Figure 19(c)**. The spectral lines in the optical domain shown in **Figure 19(a)** beat to form the RF signals shown in **Figure 19(b)**. The quality factor of the microresonator used for this measurement was 2 x 10^6 and had a diameter of 100 µm. The resonator was undercoupled in this measurement. The full width at half-maximum is about 100 MHz, so we do not expect a large number of cascaded Stokes beams.

Figure 19(d) shows the beat notes from the cascaded FSBS in the microsphere. This resembles the spectrum we expect, as shown in **Figure 19(b)** The anti-Stokes and Stokes beams generate beat notes to the left and right of the AOM drive frequency at 200 MHz, respectively. In the low frequency end, the beat notes between the anti-Stokes and the pump overlap with the beat notes between the pump and the Stokes beams. Near the AOM drive frequency, the anti-Stokes and Stokes beams are mapped to unique frequencies in the RF domain. The Stokes beams are observed to be stronger than the anti-Stokes beams. The results shown in this section shows the promise of exploring FSBS in chalcogenide resonators.

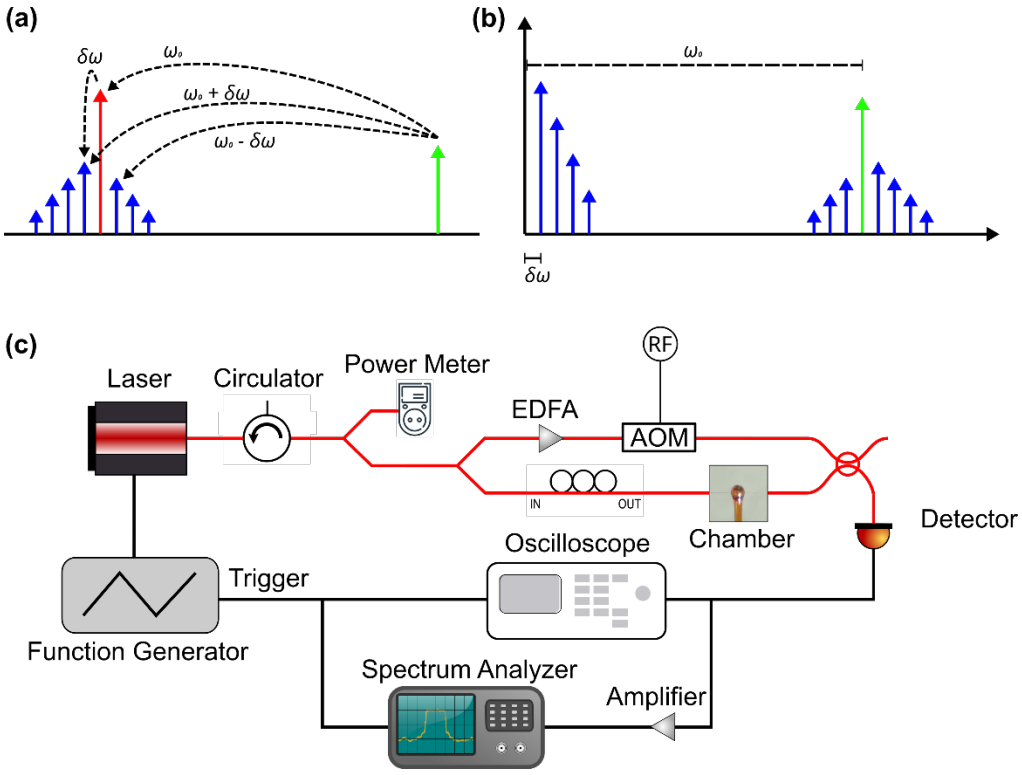

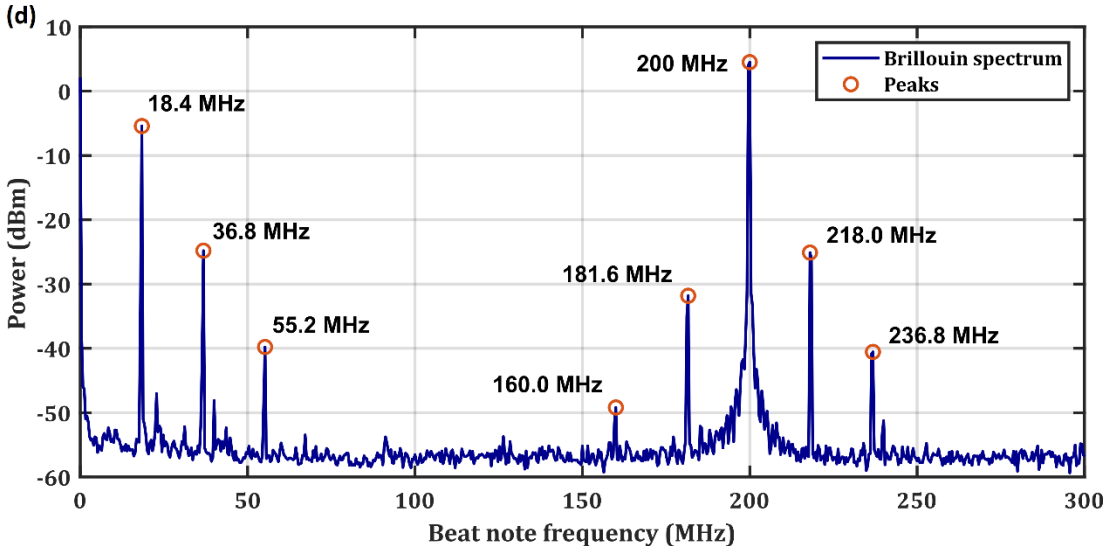

Figure 19. (a) Schematic for optical heterodyne measurement of anti-Stokes beams generated by cascaded forward Brillouin scattering. The acousto-optic modulator (AOM) generates a probe beam with a frequency 200 MHz higher than the pump frequency. The beat notes are generated at $\omega_0 \pm n\delta\omega$, where ω = 200 MHz is the drive frequency of the AOM and $\delta\omega$ is the Brillouin shift. (b) Beat notes generated between the cascaded Brillouin beams, pump beam and probe beam. The beat notes from the Stokes beams appear at a higher frequency than the AOM drive frequency. (c) Experimental setup for heterodyne measurement of anti-Stokes beams. The tunable diode at 1550 nm was coupled into a 100 µm microsphere using a tapered silica fiber and tuned into resonance. The AOM generates a heterodyne probe beam, with no modulation applied. To compensate for the relatively large insertion loss of the AOM, an Erbium-doped fiber amplifier (EDFA) was used. A 50-50 coupler was used to mix the probe beam with the signal from the resonator. The beatnotes are detected using a detector of bandwidth 1.2 GHz and measured using an RF spectrum analyzer. (d) Cascaded FSBS spectrum in a 100 µm sphere with unloaded quality factor 2 x 10^6 measured using a heterodyne probe beam. The anti-Stokes and Stokes beams generate beat notes to the left and right of the AOM drive frequency at 200 MHz, respectively. In the low frequency end, the beat notes between the anti-Stokes and the pump overlap with the beat notes between the pump and the Stokes beams. Near the AOM drive frequency, the anti-Stokes and Stokes beams are mapped to unique frequencies in the RF domain. We note that the Stokes beams are stronger than the anti-Stokes beams.

References

1. Qiu W, Rakich PT, Shin H, Dong H, Soljacic M, Wang Z. Stimulated Brillouin scattering in nanoscale silicon step-index waveguides: a general framework of selection rules and calculating SBS gain. Opt Express. 2013;21(25):31402-19. Epub 2014/02/12. doi: 10.1364/OE.21.031402. PubMed PMID: 24514715.

2. Grayson M, Xu B, Shanavas T, Zohrabi M, Bae K, Gopinath JT, Park W. Fabrication and characterization of high quality GeSbSe reflowed and etched ring resonators. Opt Express. 2022;30(17):31107-21. doi: 10.1364/oe.468249.
3. Shanavas T, Grayson M, Xu B, Zohrabi M, Park W, Gopinath JT. Cascaded forward Brillouin lasing in a chalcogenide whispering gallery mode microresonator. APL Photonics. 2022;7(11). doi: 10.1063/5.0112847.
4. Mirnaziry SR, Wolff C, Steel MJ, Morrison B, Eggleton BJ, Poulton CG. Lasing in ring resonators by stimulated Brillouin scattering in the presence of nonlinear loss. Opt Express. 2017;25(20):23619-33. Epub 2017/10/19. doi: 10.1364/OE.25.023619. PubMed PMID: 29041313.
5. Wolff C, Stiller B, Eggleton BJ, Steel MJ, Poulton CG. Cascaded forward Brillouin scattering to all Stokes orders. New Journal of Physics. 2017;19(2). doi: 10.1088/1367-2630/aa599e.

4) other achievements.
None

How were the results disseminated to communities of interest? If there is nothing significant to report during this reporting period, state "Nothing to Report."

We have the following conference papers with which we disseminated the research results to the relevant research communities.

1. M. Grayson, M. Zhorabi, K. Bae, J. Zhu, J. T. Gopinath and W. Park, "Enhancement of Third-Order Nonlinearity of Thermally Evaporated GeSbSe Waveguides Through Annealing", SPIE Photonics West, San Francisco, CA, Feb 1-6, 2020.
2. K. Bae, T. M. Horning, S. Pampel, M. Zohrabi, M. B. Grayson, J. T. Gopinath and W. Park, "On-chip high-quality Ge23Sb7S70 round-wedge resonators for broadband dispersion engineering", Conference on Laser and Electro-Optics (CLEO), May 11 - 15, 2020.
3. B. Xu, M. Grayson, T. Shanavas, J. T. Gopinath and W. Park, "Dispersion Control of High Quality Ge23Sb7S70 Reflowed Wedge Resonators", Conference on Laser and Electro-Optics (CLEO), San Jose, CA, May 15 - 20, 2023.
4. T. Shanavas, M. B. Grayson, M. Zohrabi, W. Park, and J. T. Gopinath, "Cascaded Forward Brillouin Scattering in a Chalcogenide Microsphere," *Presented at the 2022 Conference on Lasers and Electro-Optics (CLEO)* (2022).

We also carried out the following outreach activities to reach broader communities.

PIs Park and Gopinath hosted 50 fifth graders from High Peaks Elementary School for

half a day at the University of Colorado Boulder. Co-PI Gopinath gave lab tours to women in the Tech Girls program (all three from Africa), hosted the site lead for the Boulder Google site with the Women in ECEE Group and produced a podcast (https://blogs.cisco.com/sp/fascinating-laser-research-projects-you-wish-you-thought-of-part-1-of-9-cisco-optics-podcast-ep-35) about her perspectives and experiences with science in collaboration with Cisco.

Impacts

Development of the principal discipline(s) of the project

We made a significant progress toward narrow linewidth Brillouin laser based on chalcogenide materials. We developed a numerical simulation tool that can model both optical and acoustic modes in chalcogenide resonators, evaluate the overlap integral and calculate the anticipated gain and threshold values. We then proceeded to develop fabrication processes tailored for chalcogenide devices. We developed optimized etching recipe for reactive ion etching of chalcogenide thin films. We have also developed UV lithography, wet etching and reflow process for rounded-edge wedge resonators. Finally, we performed extensive optical characterizations to demonstrate high Q factors ($> 10^6$) in our chalcogenide resonators. Also, we performed SBS measurements to demonstrate strong forward Brillion scattering in a microresonator. High quality, narrow-linewidth microresonator based on chalcogenide could enable a wide array of applications in spectroscopy, metrology, communications and sensing.

Other disciplines:

The fabrication process we developed for high quality chalcogenide resonators can be readily extended for chalcogenide based integrated optical devices for many applications including, but not limited to, novel light source, navigation and quantum information technology.

Describe the impact in this reporting period on the development of human resources

The project provided research opportunities to 1 undergraduate student, 2 graduate students, 1 postdoctoral research and 1 senior scientist. These researchers gained valuable skills on numerical simulations, device fabrication and optical measurements. Also, they were all engaged in research discussions through which they developed critical abilities such as creative and independent thinking, interdisciplinary collaboration and project management.

Describe the impact on teaching and educational experiences

Interdisciplinary research opportunities for undergraduate and graduate students as well as researchers will blend research with education both in the laboratory and the classroom. The online Master's degree in Electrical Engineering that CU Boulder has recently launched features courses on both semiconductors, lasers, and detectors taught by both of the PIs.

Describe the impact in this reporting period on physical, institutional, and information

resources that form infrastructure.

None.

Impact on society beyond science and technology:

The project helped organize and execute outreach events for broader communities as reported earlier.

Changes

Changes in approach

None.

Problems or delays

There were some delays due to COVID pandemic, which led to one-year no-cost extension.

Expenditure Impacts

None.

Significant changes in the use or care of human subjects, vertebrate animals and/or biohazards

N/A

Changes to the primary place of performance from that originally proposed

None.